J Mater Sci: Mater Electron

Facile synthesis of bismuth ferrite nanoparticles for ppm-level isopropanol gas sensor

Zichen Zheng[1], Ying Li[1], Yifan Luo[1,2], Marc Debliquy[2], and Chao Zhang[1,*]

[1] College of Mechanical Engineering, Yangzhou University, Huayang West Road 196, Yangzhou 225127, People's Republic of China
[2] Service de Science des Matériaux, Faculté Polytechnique, Université de Mons, 7000 Mons, Belgium

Received: 25 May 2022
Accepted: 30 June 2022

ABSTRACT

Breath gas detection has attracted significant attention for the early screening of lung cancer. In this paper, we synthesized bismuth ferrite ($BiFeO_3$) nanoparticles via a green and facile microwave hydrothermal method for detecting low concentration isopropanol. The influence of material's synthesis process parameters, including temperature, time and power of synthesis on the physicochemical properties, has been explored. The structure, morphology and other material properties of $BiFeO_3$ were analyzed by a series of characterization methods such as scanning electron microscopy (SEM), X-ray diffraction (XRD), transmission electron microscopy (TEM) and X-ray electron spectroscopy (XPS). The effects of synthesis process parameters and testing conditions on gas sensing performance were investigated by a four-channel testing chamber. In addition, the mechanism of gas-sensitive response was also discussed. Considering the authentic situation of exhaled breath of human, we conducted the experiment of ultralow concentration and high humidity systematically. Typically, the $BiFeO_3$ gas sensor revealed extraordinary sensitive performance at an optimal working temperature of 275 °C. An excellent linear relationship existed in the response and gas concentration, as the response value can reach 3.9 towards 1 ppm isopropanol even if it is in a 100% relative humidity (RH) atmosphere.

1 Introduction

Lung cancer is one of the most common challenges around the world, whose mortality rate is rather higher than other diseases [1]. According to the report from global cancer database in 2018, more than 2.09 million people have been diagnosed with lung cancer per year, and 1.76 million people died of it [2]. Studies have shown that the long-term survival rate after surgery for stage I of lung cancer exceeds 80%, but that for stage III is only 20% [3]. The 5-year survival rate of lung cancer is only 18% at present. The important reason is that nearly 75% of patients are

Address correspondence to E-mail: zhangc@yzu.edu.cn; zhangchao_cqu@hotmail.com

https://doi.org/10.1007/s10854-022-08703-x
Published online: 11 July 2022

already in stage II and stage III of lung cancer when they are diagnosed, and the best treatment time is missed. The inability to detect and diagnose in time has dramatically increased the mortality of lung cancer [4]. If the tumor can be surgically removed early, the five-year survival rate can reach 85% [5]. The typical diagnosis methods, mainly classified into imaging examination, cytology or histopathology examination and body fluid tumor marker detection, are essential to diagnose. However, obvious deficiencies exist in these methods, such as radiation, trauma, complicated process, high technical requirements and expensive cost [6]. Therefore, a new technique with accurate, convenient, and noninvasive traits is in urgent need for the preclinical diagnosis of lung cancer.

Under pathological conditions, the composition of volatile organic compounds (VOCs) in exhaled breath will change. It is reasonable to confirm the pathophysiological state of humans by exhaled breath measurement and analysis [7]. Exhaled breath detection can be used as a safe and convenient disease diagnosis auxiliary method, which has the advantages of being simple and noninvasive [8]. In previous studies, several VOCs which can be defined as biomarkers for lung cancer, including ethanol, acetone, n-butanol and isopropanol have been reported [9]. As a monohydric alcohol, isopropanol is one of the VOCs in lung cancer patients' exhaled breath. Previous studies have found that the average concentration of isopropanol in the exhaled breath of healthy people and lung cancer patients is 169 ppb and 398 ppb, respectively, which has a great difference between the two situations [1].

In recent years, many gas sensors have served as potential tools for detecting diseases, such as colorimetric, quartz crystal microbalance, surface acoustic wave, and metal oxide semiconductor gas sensors [10]. Mazzone et al. confirmed that the colorimetric sensor arrays could identify the biomarkers for lung cancer in the exhaled breath [11]. The proton conduction sensor realized effective detection of NH_3 in exhaled breath [12]. The quartz crystal microbalance sensor studied by Xu et al. displayed excellent sensing performance for low-concentration acetone [13]. Above all, gas sensing technology is showing great potential for disease detection applications. Among the different types of gas sensors, metal oxide semiconductor gas sensor technology has the feature of low cost, high sensitivity, quick response, strong specificity and simple operation, which provides a new development idea for exhaled breath detection in disease screening and diagnosis [14–16].

Considerable interest has arisen over the area of chemistry and metal oxide semiconductor materials as the superior ferroelectric and catalytic performance of $BiFeO_3$. In the past decade, many synthesis techniques such as solid-state [17], sol–gel [18], rapid liquid-phase sintering [19], co-precipitation [20] and hydrothermal [21] methods were used to synthesize $BiFeO_3$. In addition to these methods, the microwave hydrothermal method can be used to synthesize such materials quickly, simply, uniformly and energy-saving [22]. In addition, most researches focused on ferroelectric properties of $BiFeO_3$, only few researches about the application in gas sensing field were published [23].

As the monitoring of isopropanol vapor still have drawbacks such as low response, high working temperature, and low detection limit. Therefore, it is very crucial to develop an effective sensor for isopropanol detection and improve its sensing performance. This paper reports on that isopropanol as a biomarker for lung cancer was detected by a $BiFeO_3$ gas sensor. The microwave-assisted hydrothermal method proved a one-step and fast method for preparation of $BiFeO_3$ nanoparticles. The relationship between synthesis parameters (reaction temperature, time and power) on the material's properties and the gas sensing performance to isopropanol vapor were studied.

2 Material and methods

2.1 Synthesis of $BiFeO_3$ by microwave hydrothermal

The chemicals used in the experiment were all purchased from Aladdin Biochemical Technology Co., Ltd. without further purification treatment. 2.02 g $Fe(NO_3)_3{\cdot}9H_2O$ and 2.43 g $Bi(NO_3)_3{\cdot}5H_2O$ were dissolved in 10 mL HNO_3 solution (2 mol/L). After the dissolution was complete, 10 mL sodium hydroxide solution (6 mol/L) was added dropwise to generate a brick-red precipitate. After 20 min vibrant stirring, deionized water was added for rinsing the precipitate. The obtained solution was subjected to ultrasonic treatment and placed in a microwave hydrothermal synthesizer to react for the 30 min at

200 °C and 500 W to obtain the $BiFeO_3$ material which can be defined as BFO-MW. The simplified synthesis steps are shown in Fig. 1. When exploring the influence of synthesis procedure conditions on material properties, the predetermined reaction parameter needs to be changed (Table 1), and all other conditions must remain the same. Then the above experimental steps should be repeated to obtain materials with different synthetic parameters.

To further explore the characteristics of microwave hydrothermal synthesis and the feature of $BiFeO_3$, similar experiments were carried out under ordinary hydrothermal conditions. The previous steps are consistent with the microwave hydrothermal method. After rinsing by deionized water, the obtained solution was transfered into a stainless steel autoclave with a Teflon liner of 50 mL capacity and heated at 200 °C for 12 h. When it comes down to room temperature, the precipitate obtained was washed with deionized water and ethanol for several times. Then, the precipitate was dried for 8 h in an oven at 80 °C. This material is denoted as BFO-HY.

2.2 Characterization

The diffraction of X-rays (XRD, D8 Advance Bruker) was used to analyze the phase structure of $BiFeO_3$, and the Cu-$K_{\alpha 1}$ radiation is chosen and the scanning rate is set as $5°{\cdot}min^{-1}$. The morphologies were obtained from the observation results of field-emission scanning electron microscopy (FESEM, S4800II Hitachi) and transmission electron microscopy (TEM, JEM-2100). X-ray photoelectron spectroscopy (XPS, Thermo Fisher Scientific ESCALAB 250Xi) was used for determining the chemical states of the elements in $BiFeO_3$. The specific surface areas were acquired through N_2 adsorption/desorption at 300 °C according to BET theory. The pore sizes of samples were calculated by BJH (Barret–Joyner–Halenda) method using the isotherms (Autosorb IQ3, Quantachrome Instruments).

Table 1 Different microwave process parameters

Number	Temperature/°C	Time/min	Power/W
1	125	30	500
2	150	30	500
3	175	30	500
4	200	30	500
5	225	30	500
6	250	30	500
7	200	10	500
8	200	50	500
9	200	30	100
10	200	30	300
11	200	30	700
12	200	30	900

2.3 Fabrication and measurement of sensors

The experimental equipment was built by laboratory personnel which have been reported via the other papers written by our research group [24, 25]. It contained air intake system and signal processing system, as shown in Fig. 2. High pure air was purchased from Yangzhou Ruite Gas company limited and mass flow controllers (Bronkhorst, F-201CV-1K0-RGD-33-V and F-201CV-050-RGD-33-V) were obtained from Beijing Artim Control Equipment company limited. The gas-sensing detection system adopts home-made four-channel testing system.The Pt/Au heating electrodes and gas testing chamber (HCRK-SD101, China) were purchased from Wuhan Huachuang Ruike Technology company limited. By

Fig. 1 The synthetic schematic of $BiFeO_3$

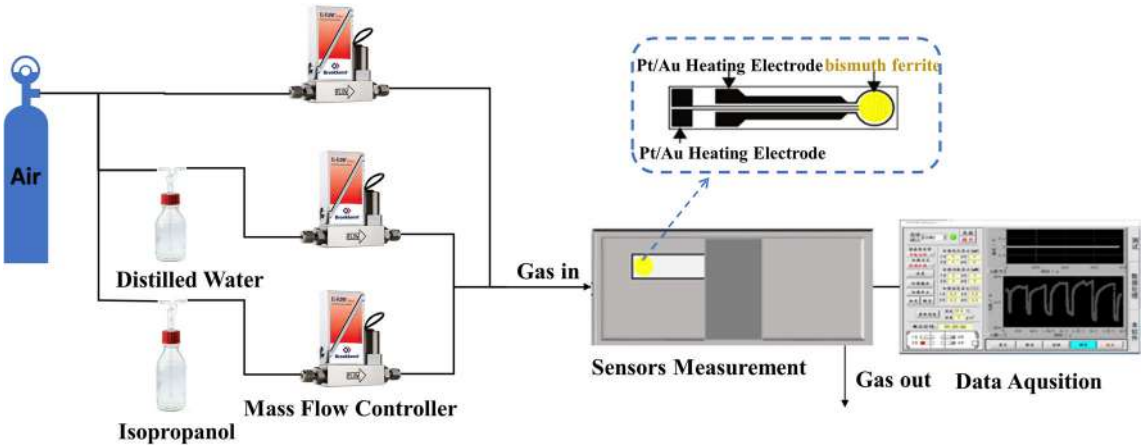

Fig. 2 The four-channel gas sensitivity testing system

dropping the as-prepared $BiFeO_3$ onto the electrodes, and drying the electrodes at 80 °C for 12 h, the $BiFeO_3$ gas sensor was made. The concentration of isopropanol vapor was adjusted by mass flow controllers and the specific control details can be found in the supplementary materials and our previous studies [26]. The changes of electrical resistance of the fabricated sensors were recorded via the home-made signal processing system. Besides, the gas-sensitive response value S was defined as the ratio of the resistance value of the semiconductor material in the target gas (R_g) and in the standard air (R_a), $S = R_g/R_a$ [27]. The response or recovery time was defined as the resistance change of gas sensor reached 90% of (R_g-R_a) [28]. Gas sensing experiments were carried out under laboratory conditions with a room temperature of 25 ± 2 °C and of 30 ± 10% RH.

3 Results and discussion

3.1 XRD and TEM analysis

To study the effect of microwave synthesis process on the properties of materials, $BiFeO_3$ powders synthesized at 125, 150, 175, 200, 225 and 250 °C for 30 min and 500 W were analyzed by XRD. As shown in Fig. 3a, when the reaction temperature is below 200 °C, the phase composition is mainly $Bi_{25}FeO_{40}$. The diffraction peaks with 2θ at 24.7, 27.7, 30.5, 32.9, 35.6, 39.7, 41.7, 52.5, 54.2, 55.8 and 62.0° were observed in this case, which related to the sillenite-type phase of $Bi_{25}FeO_{40}$ (JCPDS 46–0416) [29]. With the increase of temperature, pure $BiFeO_3$ is easier to form, and diffraction peaks with 2θ at 22.4, 27.7, 31.7, 32.1, 39.0, 39.5, 45.8, 56.5 and 57.1° were observed, which was assigned to the perovskite phase of $BiFeO_3$ (JCPDS 86–1518, ICSD #82,614) [30]. With the increasing reaction temperature, the degree of dissolution of the precursor was promoted, which is beneficial to reach the critical supersaturation point for the formation of $BiFeO_3$. Ponzoni et al. pointed out that the reaction temperature exerts a significant influence on the formation of $BiFeO_3$ by affecting the dissolution–recrystallization process. Only when the ion concentration in the alkaline environment reached the saturation point, the thermodynamically stable $BiFeO_3$ phase started nucleating and growing [31]. With the increasing reaction temperature, grain growth direction and selectively oriented crystal planes changed. The diffraction peak intensity at 2θ = 27.7° of the samples synthesized in the temperature range of 125–175 °C gradually became stronger, indicating that the grains grow along the (310) crystal plane with the increasing temperature. In the range of 200 to 250 °C, the diffraction peak at 2θ = 22.4° becomes stronger, and the grains grow along the (101) and (202) crystal planes. In addition, by comparing the XRD patterns of the samples synthesized by microwave-assisted hydrothermal method and ordinary hydrothermal method, it can be found that the BFO-HY sample has impure phase composition and contains at least two phases, $BiFeO_3$ and $Bi_2Fe_4O_9$, as depicted in Fig. 3b. In the research of Wang et al. on the microwave-assisted synthesis of $BiFeO_3$ nanoparticles, the materials synthesized by microwave have higher crystallinity than those synthesized by the hydrothermal method [32].

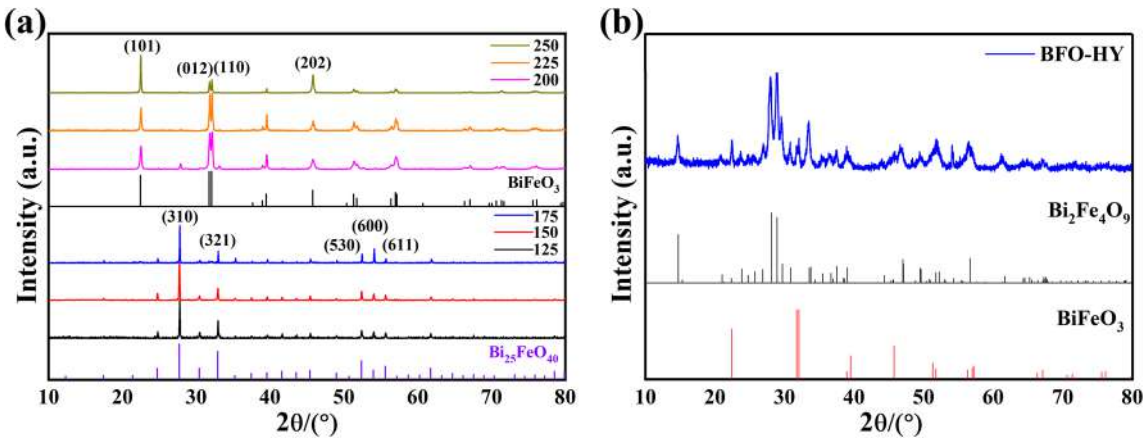

Fig. 3 X-ray diffraction patterns of $BiFeO_3$ synthesized under different conditions: **a** $BiFeO_3$ synthesized at 125, 150, 175, 200, 225 and 250 °C; **b** $BiFeO_3$ synthesized by traditional hydrothermal method

The sample morphology was observed, and the TEM images indicate that the $BiFeO_3$ products mainly consist of nanoparticles of around 3 nm when the temperature is between 125 and 200 °C. Furthermore, as the temperature is between 200–250 °C, it gradually transforms into a cubic structure. The existence of hexagons can be observed in the electron microscope of materials synthesized at 250 °C, as shown in Fig. 4. With the increase of temperature, the particle size of nanostructures gradually increases.

It has been reported that the reaction time affects the phase composition of $BiFeO_3$ [22]. Three samples were prepared by reacting at 200 °C for 10 min, 30 min, and 50 min with a power of 500 W for exploring the impact of reaction time on material properties. From the XRD patterns in Fig. 5a, it can be found that when the reaction time is 10 min, the phase composition includes $Bi_{25}FeO_{40}$ and $BiFeO_3$. As the reaction time prolonged to 30 min, the characteristic peaks (2θ = 24.8°, 27.8°, 30.6°, 33.1°) belonging to the impurity phase $Bi_{25}FeO_{40}$ weakened or even disappeared, and $BiFeO_3$ became the main phase. If the reaction time continued to extend to 50 min, the intensity of the peaks related to the impurity phases increased again, which is consistent with the phenomenon found by Chen et al. [33]. With the prolongation of reaction time, the impurity phase has a state change of existence-disappearance-existence. The formation of impurity phases may be related to the decomposition and regeneration of $BiFeO_3$, as shown in Eq. (1) [22].

$$6BiFeO_3 \rightarrow 2Bi_2O_3 + Bi_2Fe_4O_9 + Fe_2O_3 \quad (1)$$

Under the condition of keeping the reaction temperature and time consistent, different microwave powers (100 W, 500 W, 900 W) were used to synthesize $BiFeO_3$. Comparing the XRD patterns in Fig. 5b, it is clear that the peak position of the synthesized sample is not obvious when the power is 100 W, while the broadening is obvious and the peak is weak, indicating that the crystallinity of this sample is poor. After the power was increased, the diffraction pattern of the material became sharper. When the power increases further, the grains grow along the (310) crystal plane of $Bi_{25}FeO_{40}$. Therefore, the corresponding diffraction peak of 27.7° becomes strong, while the diffraction peaks corresponding to the two crystal planes (012) and (110) of $BiFeO_3$ become weak. The previous study of Majid et al. also showed that the increase of microwave power would make the particle crystal size decrease and the crystallinity increase [34].

3.2 SEM, BET and XPS analysis

The $BiFeO_3$ in the form of nanoparticles was observed by SEM in Fig. 6a, which was in accordance with the images from TEM. Through N_2 adsorption–desorption experiments, the specific surface area of the as-synthesized BFO-MW was 56.1 $m^2 \cdot g^{-1}$ under the conditions of 200 °C and 500 W for 30 min, as shown in Fig. 6b. The material has a large specific surface area, which can offer more reaction sites for gas molecule adsorption, accelerating the gas-sensing reaction. We define the selected $BiFeO_3$ with the microwave power of 500 W at 200 °C for 30 min synthesis process parameters as BFO-MW1.

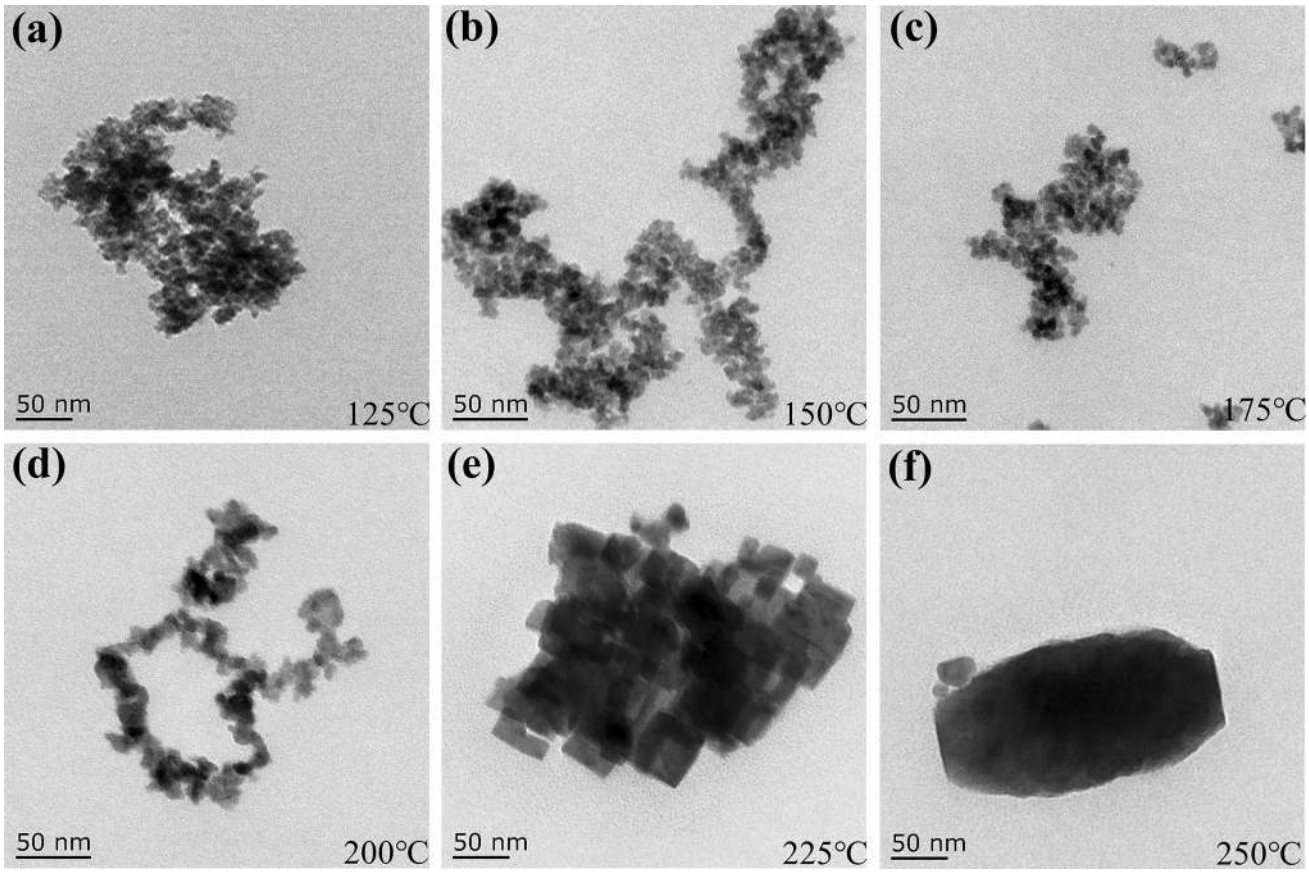

Fig. 4 TEM images of $BiFeO_3$ synthesized at **a** 125 °C; **b** 150 °C; **c** 175 °C; **d** 200 °C; **e** 225 °C and **f** 250 °C

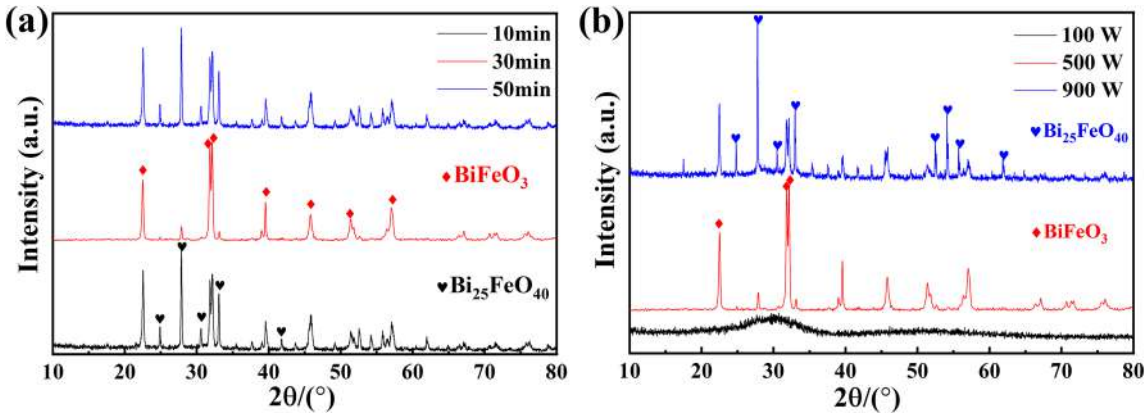

Fig. 5 **a** XRD patterns of $BiFeO_3$ synthesized with different microwave reaction times (10, 30 and 50 min); **b** XRD patterns of $BiFeO_3$ synthesized with different microwave powers (100, 500 and 900 W)

To analyze the elemental composition and element valence state of the material surface, XPS tests were carried out on the material and the results are depicted in Fig. 7, the binding energy of the samples synthesized by different methods showed that the survey is in the range of 0.0–1000.0 eV. The XPS results indicated three elements Bi, Fe, and O exist on the material surface, and BFO-HY has the same peak positions as BFO-MW1. It showed that BFO-HY and BFO-MW1 are composed of the same elements and valence states (Fig. 7a). The two peak positions of the Bi $4f_{7/2}$ and Bi $4f_{5/2}$ spectrum are at 158.5 and 163.9 eV (Fig. 7b), corresponding to Bi^{3+} [35]. The positions of the two peaks ($2p_{3/2}$ and $2p_{1/2}$) of Fe in

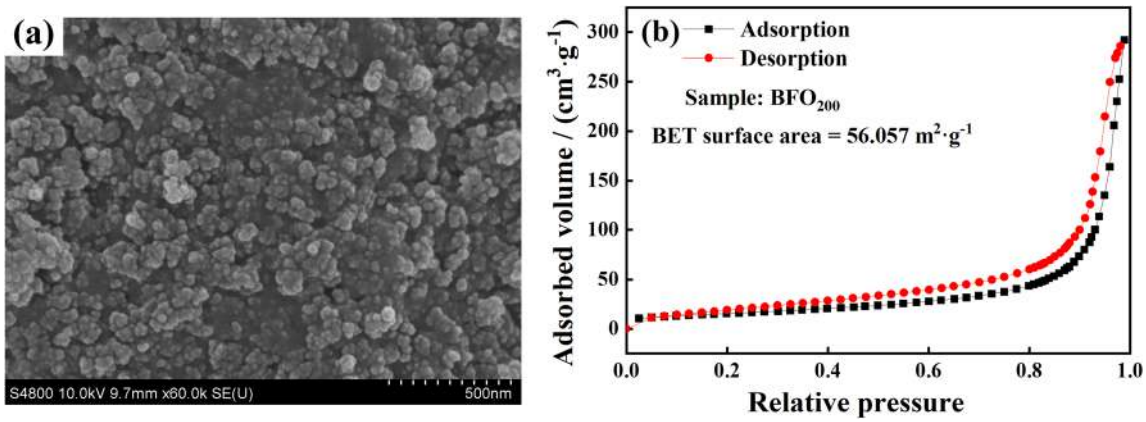

Fig. 6 $BiFeO_3$ synthesized under the microwave power of 500 W and 200 °C for 30 min of **a** SEM image; **b** N_2 adsorption–desorption curve

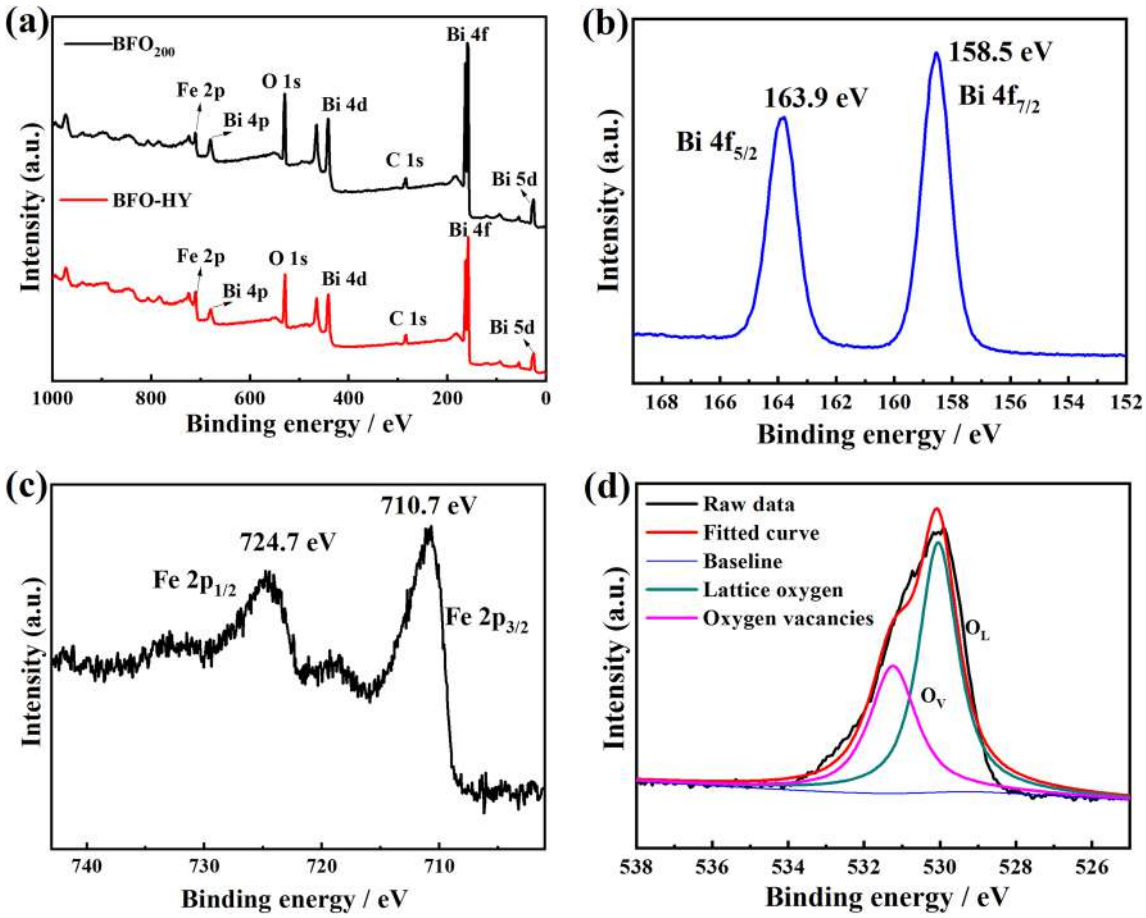

Fig. 7 **a** XPS survey spectrum of BFO-HY and BFO-MW1; High-resolution XPS spectra related to **b** Bi 4f; **c** Fe 2p and **d** O 1 s of BFO-MW1

the spectrum indicate the presence of Fe^{3+} (Fig. 7c). The high-resolution spectrum of O has two sub-peaks. The 529.5 eV and 531.8 eV peaks correspond to lattice oxygen field and oxygen vacancies field (Fig. 7d) [36]. The proportion of oxygen vacancies calculated from the integral area is 38.2%. The chemical adsorption of oxygen exerts an important impact to the surface reaction with the target gas. The

larger the proportion of the chemical adsorption of oxygen, the better the gas sensing performance of the material.

3.3 Gas-sensing performance

The 125, 150, 175, 200, 225 and 250 °C synthesized $BiFeO_3$ gas sensors were evaluated at different working temperatures (200, 225, 250, 275, 300 and 325 °C) under 5 and 10 ppm isopropanol and the RH of the surrounding environment was about 35%. The working temperature of the sensor affects the gas-sensing performance by affecting the gas diffusion process and reaction process [37]. It is found that all $BiFeO_3$ samples have the highest gas-sensing response at the 275 °C testing condition, as shown in Fig. 8a. The $BiFeO_3$ synthesized at 200 °C can detect 5 ppm isopropanol with a response of 6. At the optimum working temperature of 275 °C, gas-sensing tests were carried out on $BiFeO_3$ materials synthesized by different processes.

The samples with the synthesis temperature range of 125–250 °C show different gas-sensing properties under the same test conditions (275 °C). Among them, the $BiFeO_3$ synthesized at 200 °C presented the highest response to 10 ppm isopropanol, with a value of 14.1, significantly higher than that of other samples shown in Fig. 8b, c.

In the experiment on the influence of power parameters, the gas sensing performance of samples synthesized at 100 W was poor, and the response improved when the power increased as a whole, as shown in Fig. 8d. The gas sensitivity test was carried out for samples with different reaction times (10, 30 and 50 min) as well, which is depicted in Fig. 8e, f, and the 30-min sample showed better gas sensing performance and higher sensitivity. Above all, 500 W, 200 °C and 30 min are the overall best synthesis parameters, which are consistent with XRD results.

Exhaled breath detection conditions are harsh, while the breath contains a large amounts of water molecules and the ultra-low concentration of the biomarkers. Therefore, this paper simulates exhaled breath detection under experimental conditions. The synthetic materials with the best gas-sensing properties (BFO-MW1) were selected from the above samples for simulation experiments. The BFO-MW1 gas sensor was prepared for the gas-sensing research under the optimal working temperature (275 °C), and the results for low-concentration (0.2–1 ppm) isopropanol vapor are shown in Fig. 9a, b. Under the condition of 80% RH, BFO-MW1 showed excellent gas-sensing performance, which still had a high response value (3.62) to 0.2 ppm isopropanol, and the response value and concentration had an excellent linear relationship. In addition, BFO-MW1 gas sensor responds quickly to low concentrations of isopropanol. It only takes 45 s and 14 s to respond to ultra-low concentrations of 0.2 ppm (Fig. 9c) and 1 ppm isopropanol (Fig. 9d), and it also reveals a good recovery speed (118 s and 58 s).

Humidity affects the overall gas-sensing properties of materials by affecting the adsorption of oxygen on the material surface [38]. Figure 10a, b shows the comparison of the response of BFO-MW1 sensor to 1 ppm isopropanol under different humidity conditions. As the humidity increases, the response value decreases. By feeding only wet air to the gas-sensitive test system, RH can be adjusted to 100%. However, even at 100% RH, which is close to the humidity in human exhaled breath, $BiFeO_3$ still has good sensitivity to 1 ppm isopropanol, with a response value of 3.9.

The selectivity of the gas sensor to the target gas is an important indicator for the sensor to be used for disease detection. Further selectivity tests of BFO-MW1 sensor were carried out, as shown in Fig. 10c. BFO-MW1 sensor has low sensitivity to methane, carbon dioxide, NH_3, hydrogen, nonanal, ethanol and acetone. Meanwhile, $BiFeO_3$ shows excellent repeatability and long-term stability, as shown in Fig. 10d to Fig. 10f. The changes in response values towards 1 ppm isopropanol did not exceed 5% for BFO-MW1 gas sensor, indicating that the BFO-MW1 gas sensor can keep a stable response for at least half a month. Compared with the performance of other isopropanol metal oxide semiconductor sensors, as shown in Table 2, the as-prepared $BiFeO_3$ gas sensor exhibits excellent gas-sensing performance, which has a lower operating temperature, an ultra-low detection limit, and has considerable application prospects for breath gas detection.

3.4 Gas-sensing mechanism

Gas-sensing reactions are generally accounted for the physical and chemical reactions of gas molecules on the surface of sensing layers. $BiFeO_3$ gas sensor is a p-type semiconductor gas sensor based on the electrical

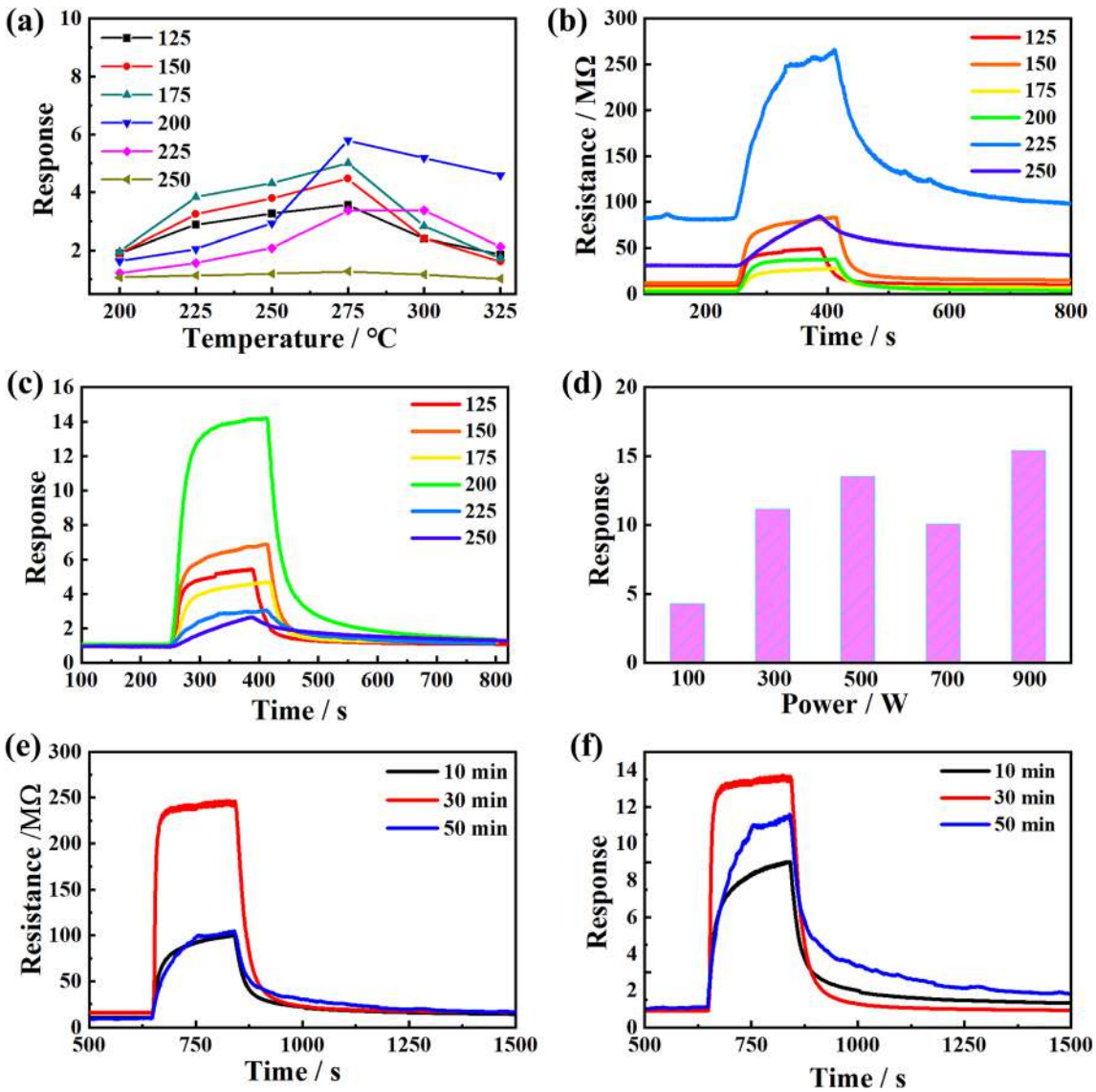

Fig. 8 **a** Responses of 125, 150, 175, 200, 225 and 250 °C synthesized materials to 5 ppm isopropanol at different working temperatures (200, 225, 250, 275, 300 and 325 °C); **b** resistance and **c** response curve of synthesized materials under different temperature conditions to 10 ppm isopropanol at the optimal working temperature; **d** response comparison of synthesized materials to 10 ppm isopropanol under different power (100, 300, 500, 700 and 900 W); **e** resistance and **f** response curve of synthesized materials in response to 10 ppm isopropanol at different reaction time (10, 30 and 50 min)

resistance change of the material, and the there are existing gas molecule adsorption and desorption onto the $BiFeO_3$ surface in different atmospheres. A lot of researches have been focusing on $BiFeO_3$ due to its intrinsic and relatively low bandgap (2.67–3.1 eV) [45]. Taking the $BiFeO_3$ of 2.8 eV for example, the schematic diagram of gas sensing mechanism is shown in Fig. 11. When the gas-sensitive material is in air, the oxygen molecules adsorbed on the surface of $BiFeO_3$, converted into oxygen ions after the electrons are taken from the material surface [46]. The ionized adsorption of oxygen on $BiFeO_3$ leads to hole-accumulation layers (HALs) [47]. Therefore, the electron concentration on the surface of the material increases, and the hole concentration increases, resulting to the decline of material resistance. The process of oxygen adsorption and ionization on the material surface is affected by temperature. In general, the ionosorption species of O_2^-, O^-, and O^{2-} are dominant at < 200 °C, between 200 and 300 °C, and at > 300 °C, respectively, as shown in Eqs. (2–5). [26, 48, 49].

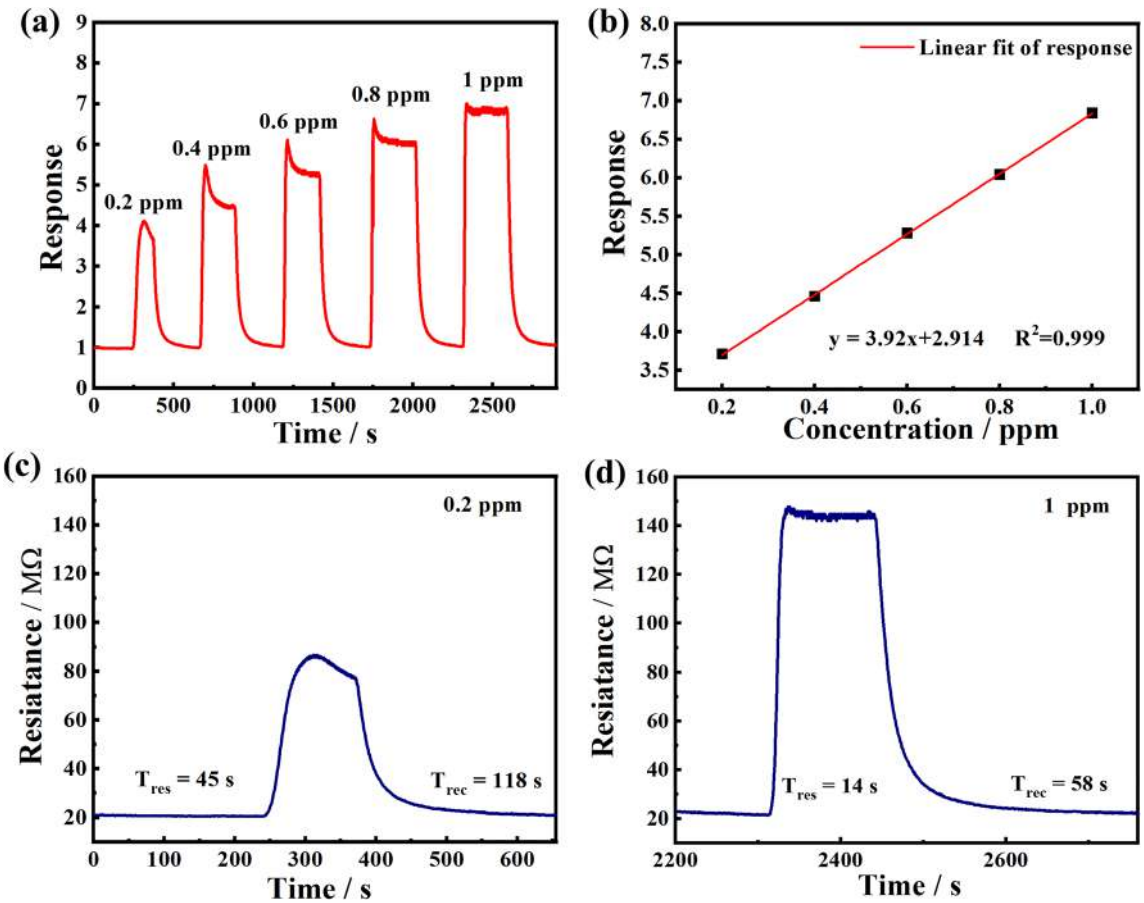

Fig. 9 **a** Response curve and **b** response–concentration linear relationship of BFO-MW1 to low concentrations of isopropanol vapor (0.2 ppm—1 ppm) at 275 °C under 80% RH; response/recovery process of BFO-MW1 gas sensor to **c** 0.2 ppm and **d** 1 ppm isopropanol vapor at 275 °C under 80% RH

$$O_2(gas) \rightarrow O_2(ads) \quad (2)$$

$$O_2(ads) + e^- \rightarrow O_2^-(<200\,^\circ C) \quad (3)$$

$$O_2(gas) + 2e^- \rightarrow 2O^-(200-300\,^\circ C) \quad (4)$$

$$O^-(ads) + e^- \rightarrow O^{2-}(>300\,^\circ C) \quad (5)$$

When isopropanol enters the test chamber, isopropanol molecules will contact with reactive oxygen ions to generate CO_2 and H_2O, releasing free electrons, and the hole concentration on the surface of the material will decrease, causing the resistance value to increase. When it is in the air environment again, the resistance value of the material will decrease due to a large amount of adsorption of oxygen. The general reaction Eqs. (6–9) are as follows [50]:

$$C_3H_8O(gas) \rightarrow C_3H_8O(ads) \quad (6)$$

$$C_3H_8O(ads) + 9O^-(ads) \rightarrow 3CO_2(gas) + 4H_2O(gas) + 9e^- \quad (7)$$

$$C_3H_8O(ads) + 9O_2^-(ads) \rightarrow 3CO_2(gas) + 4H_2O(gas) + 18e^- \quad (8)$$

$$e^- + h^+ \rightarrow Null \quad (9)$$

The air contains a certain amount of water molecules, and the water molecules will also be adsorbed on the surface of the material, occupying the reaction sites, and forming a competitive relationship with oxygen [51]. The number of water molecules in dry air is small, and the adsorption of oxygen on the material surface is not hindered. When the humidity increases, the number of water molecules increases, while the water molecules compete with oxygen for adsorption sites, hindering the chemical adsorption of oxygen and reducing the amount of oxygen adsorption. In the gas-sensitive layer, the electron consumption decreases while the electron concentration increases and the hole concentration decreases, therefore, the reference resistance value of the

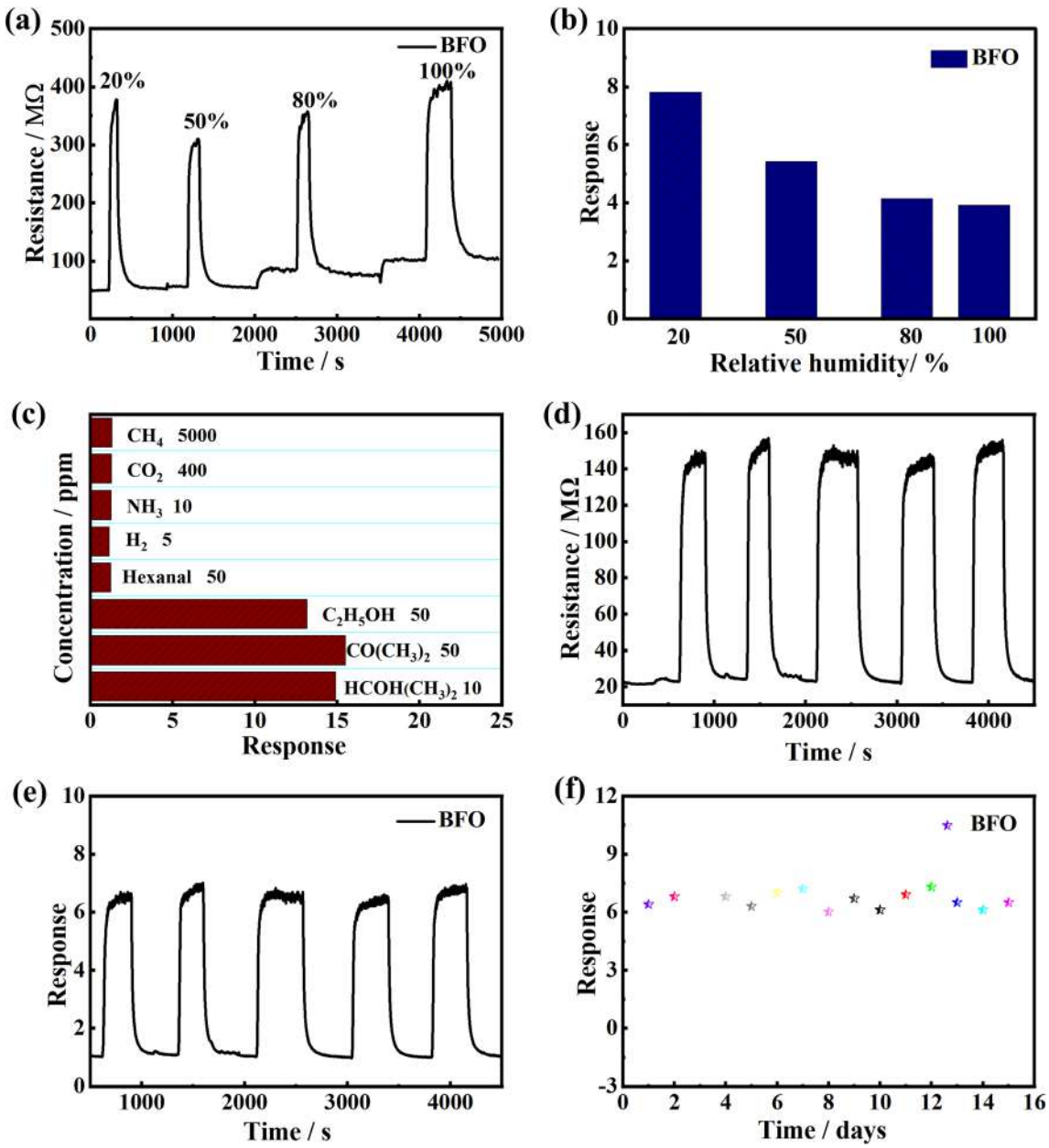

Fig. 10 **a** Response curve and **b** response value of BFO-MW1 gas sensor to 1 ppm isopropanol at 275 °C and different humidity (20%, 50%, 80% and 100% RH); **c** response of BFO-MW1 gas sensor to different types and concentrations of gases at 275 °C under 80% RH; **d** five cycles of resistance curve, **e** response curve and **f** half-month stability of BFO-MW1 gas sensor to 1 ppm isopropanol at 275 °C under 80% RH

material increases, and the response value of the target molecule decreases.

4 Conclusion

In this paper, $BiFeO_3$ was synthesized by the microwave-assisted hydrothermal method, and the factors affecting the synthesis conditions on the material microstructure was studied. The pure phase $BiFeO_3$ can be formed only when the temperature reaches about 200 °C based on XRD patterns. At the same time, the material morphology changes as synthesis temperature increases. When the temperature is in range of 150–200 °C, the material is in the form of fine nanoparticles. After the temperature gradually increases to 225 °C, the $BiFeO_3$ begins to have a cubic

Table 2 Performance comparison of isopropanol metal oxide semiconductor sensors

Sensing materials	concentration	Operating temperature	Response	Refs
SnO_2 nanorods	100 ppm	325 °C	12	[39]
PbO-doped SnO_2	500 ppm	350 °C	16	[40]
CdS/ZnO	10 ppm	320 °C	6.97	[41]
Fe-ZnO	0.25 ppm	275 °C	3.95	[26]
ZnO/NiO	20 ppm	280 °C	8	[42]
g-C_3N_4/SnO_2	1 ppm	200 °C	4.61	[43]
Ag–In_2O_3	1 ppm	300 °C	3.2	[44]
$BiFeO_3$ Nanoparticles	10 ppm	275 °C	14.1	This work

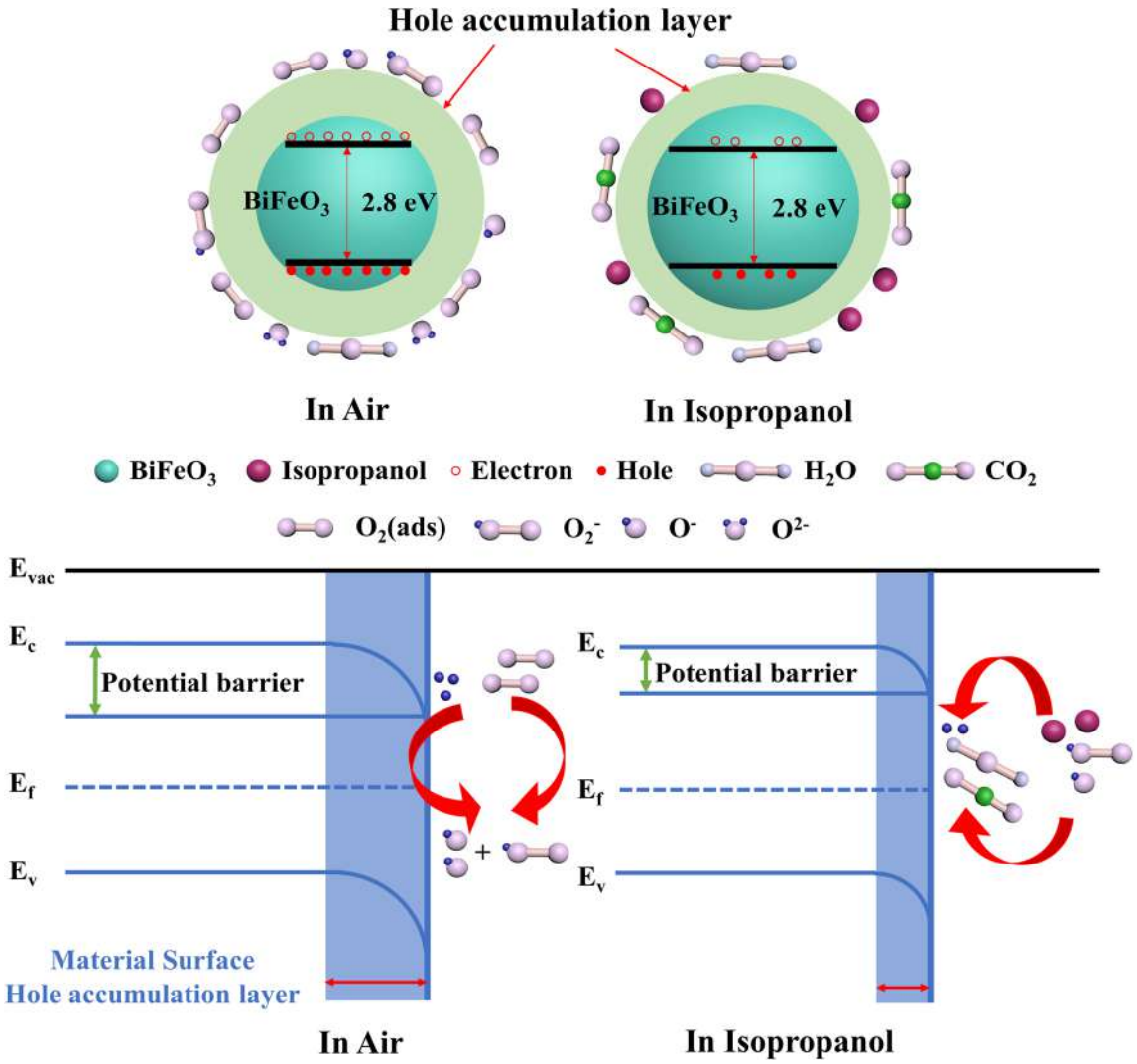

Fig. 11 Schematic diagram of the gas-sensing mechanism for the $BiFeO_3$ gas sensor towards isopropanol gas

structure. The presence of hexagonal structures can be observed at 250 °C. The length of the reaction time also affects the phase composition. As the reaction time increases from 10 to 50 min, the impurity phase will undergo the process of existence-disappearance-existence. The material obtained by the synthetic parameters of 500 W at 200 °C for 30 min has the best gas-sensing performance, and it has good sensitivity to the lung cancer marker VOCs isopropanol. Anti-humidity performance of the material was also

displayed. Even at 100% RH, the sensor still has a response value of 3.9 to 1 ppm isopropanol. On account of the $BiFeO_3$ gas sensor operating in a high humidity environment with a good stability and capable of realizing excellent response for ultralow concentration of isopropanol, $BiFeO_3$ is a promising material for the development of devices utilized in medical respiratory detection, especially in preclinical diagnosis of lung cancer.

Author contributions

All authors contributed to the study conception and analysis. Material preparation, data collection, and analysis were performed by ZZh and YL. The first draft of the manuscript was written by ZZh and YL. YL and MD edited the entire draft. CZ supervised the whole work and edited the manuscript. All authors read and approved the final manuscript.

Funding

This study was financially supported by the Outstanding Youth Foundation of Jiangsu Province of China under Grant No. BK20211548, the National Natural Science Foundation of China under Grant No. 51872254 and the National Key Research and Development Program of China under Grant No. 2017YFE0115900.

Data availability

The datasets generated during the current study are available from the corresponding author on reasonable request.

Declarations

Conflict of interest The authors declare no competing financial interest.

Supplementary Information: The online version contains supplementary material available at https://doi.org/10.1007/s10854-022-08703-x.

References

1. B. He, H.Y. Jin, Y.W. Wang, C.M. Fan, Y.F. Wang, X.C. Zhang, J.X. Liu, R. Li, J.W. Liu, Rare. Met. **41**, 132–143 (2022). https://doi.org/10.1007/s12598-021-01762-9
2. J. Ferlay, M. Colombet, I. Soerjomataram, C. Mathers, D.M. Parkin, M. Pineros, A. Znaor, F. Bray, Int. J. Cancer. **144**, 1941–1953 (2019). https://doi.org/10.1002/ijc.31937
3. C. Allemani, T. Matsuda, V. Di Carlo, R. Harewood, M. Matz, M. Niksic, A. Bonaventure, M. Valkov, C.J. Johnson, J. Esteve, O.J. Ogunbiyi, G. Azevedo e Silva, W.-Q. Chen, S. Eser, G. Engholm, C.A. Stiller, A. Monnereau, R.R. Woods, O. Visser, G.H. Lim, J. Aitken, H.K. Weir, M.P. Coleman, C.W. Grp, Lancet **391**, 1023–1075 (2018). https://doi.org/10.1016/S0140-6736(17)33326-3s
4. Y.L. Liu, Y.H. Sun, Y. Zhao, C.L. Li, F.L. Zhao, X.H. Yao, R.Q. Hang, P.K. Chu, Rare. Met. **41**, 78–85 (2022). https://doi.org/10.1007/s12598-021-01707-2
5. M.F. Reed, M. Molloy, E.L. Dalton, J.A. Howington, Am. J. Surg. **188**, 598–602 (2004). https://doi.org/10.1016/j.amjsurg.2004.07.037
6. Z. Khatoon, H. Fouad, H.K. Seo, M. Hashem, Z.A. Ansari, S.G. Ansari, J. Mater. Sci. Mater. Electron. **31**, 15751–15763 (2020). https://doi.org/10.1007/s10854-020-04137-5
7. J.E. Szulejko, M. McCulloch, J. Jackson, D.L. McKee, J.C. Walker, T. Solouki, IEEE Sens. J. **10**, 185–210 (2010). https://doi.org/10.1109/jsen.2009.2035669
8. K. Rezaei, S. Nasirian, J. Mater. Sci. Mater. Electron. **32**, 5199–5214 (2021). https://doi.org/10.1007/s10854-021-05251-8
9. M. Salimi, S. Hosseini, Sens. Actuators, B **344**, 130127 (2021). https://doi.org/10.1016/j.snb.2021.130127
10. G. Konvalina, H. Haick, Acc. Chem. Res. **47**, 66–76 (2014). https://doi.org/10.1021/ar400070m
11. P.J. Mazzone, X.-F. Wang, Y. Xu, T. Mekhail, M.C. Beukemann, J. Na, J.W. Kemling, K.S. Suslick, M. Sasidhar, J. Thorac. Oncol. **7**, 137–142 (2012). https://doi.org/10.1097/JTO.0b013e318233d80f
12. H. Zhao, L. Liu, X. Lin, J. Dai, S. Liu, T. Fei, T. Zhang, Acs. Sens. **5**, 346–352 (2020). https://doi.org/10.1021/acssensors.9b01763
13. D. Zhang, Y. Fan, G. Li, W. Du, R. Li, Y. Liu, Z. Cheng, J. Xu, Sens. Actuators, B. **302**, 127187 (2020). https://doi.org/10.1016/j.snb.2019.127187
14. Y. Li, Y.L. Lu, K.D. Wu, D.Z. Zhang, M. Debliquy, C. Zhang, Rare Met. **40**, 1477–1493 (2021). https://doi.org/10.1007/s12598-020-01557-4
15. D. Zhang, Z. Yang, S. Yu, Q. Mi, Q. Pan, Coord. Chem. Rev. **413**, 213272 (2020). https://doi.org/10.1016/j.ccr.2020.213272

16. D. Zhang, Y. Yang, Z. Xu, D. Wang, C. Du, J. Mater. Chem. A **10**, 10935–10949 (2022). https://doi.org/10.1039/d2ta01788a
17. H. Zhang, W. Jo, K. Wang, K.G. Webber, Ceram. Int. **40**, 4759–4765 (2014). https://doi.org/10.1016/j.ceramint.2013.09.020
18. T.-F. Cao, J.-Q. Dai, X.-W. Wang, Ceram. Int. **46**, 7954–7960 (2020). https://doi.org/10.1016/j.ceramint.2019.12.016
19. Y. Hong, J. Li, H. Bai, Z.J. Song, M. Wang, Z.X. Zhou, J. Adv. Ceram. **9**, 641–646 (2020). https://doi.org/10.1007/s40145-020-0398-1
20. H. Xie, K. Wang, Y. Jiang, Y. Zhao, X. Wang, Synth. React. Inorg. M. **44**, 1363–1367 (2014). https://doi.org/10.1080/15533174.2013.801859
21. G. Dong, H. Fan, Z. Cheng, S. Zhang, Ceram. Int. **46**, 26205–26209 (2020). https://doi.org/10.1016/j.ceramint.2020.06.306
22. Z. Wang, J.Y. Zhu, W.F. Xu, J. Sui, H. Peng, X.D. Tang, Mater. Chem. Phys. **135**, 330–333 (2012). https://doi.org/10.1016/j.matchemphys.2012.04.053
23. S.Z. Wu, Y. Wu, S.Q. Yin, X.G. Xu, J. Miao, Y. Jiang, Rare Met. **36**, 32–36 (2017). https://doi.org/10.1007/s12598-016-0697-4
24. K.D. Wu, J.Y. Xu, M. Debliquy, C. Zhang, Rare Met. **40**, 1768–1777 (2021). https://doi.org/10.1007/s12598-020-01609-9
25. C. Zhang, Y. Li, G.F. Liu, H.L. Liao, Rare Met. **41**, 871–876 (2022). https://doi.org/10.1007/s12598-021-01840-y
26. Y. Luo, A. Ly, D. Lahem, C. Zhang, M. Debliquy, J. Mater. Sci. **56**, 3230–3245 (2021). https://doi.org/10.1007/s10853-020-05453-1
27. S.P. Subin David, S. Veeralakshmi, M. Sakthi Priya, S. Nehru, S. Kalaiselvam, J. Mater. Sci. Mater. Electron. **33**, 11498–11510 (2022). https://doi.org/10.1007/s10854-022-08124-w
28. K. Wu, C. Zhang, J. Mater. Sci. Mater. Electron. **31**, 7937–7945 (2020). https://doi.org/10.1007/s10854-020-03332-8
29. C. Chen, J.R. Cheng, S.W. Yu, L.J. Che, Z.Y. Meng, J. Cryst. Growth **291**, 135–139 (2006). https://doi.org/10.1016/j.jcrysgro.2006.02.048
30. A. Hardy, S. Gielis, H. Van den Rul, J. D'Haen, M.K. Van Bael, J. Mullens, J. Eur. Ceram. Soc. **29**, 3007–3013 (2009). https://doi.org/10.1016/j.jeurceramsoc.2009.05.018
31. C. Ponzoni, R. Rosa, M. Cannio, V. Buscaglia, E. Finocchio, P. Nanni, C. Leonelli, J. Alloys Compd. **558**, 150–159 (2013). https://doi.org/10.1016/j.jallcom.2013.01.039
32. S. Li, G. Zhang, H. Zheng, N. Wang, Y. Zheng, P. Wang, Rsc. Adv. **6**, 82439–82446 (2016). https://doi.org/10.1039/c6ra12728b
33. W. Cao, Z. Chen, T. Gao, D. Zhou, X. Leng, F. Niu, Y. Zhu, L. Qin, J. Wang, Y. Huang, Mater. Chem. Phys. **175**, 1–5 (2016). https://doi.org/10.1016/j.matchemphys.2016.02.067
34. F. Majid, S. Riaz, S. Naseem, J. Sol-Gel. Sci. Technol. **74**, 310–319 (2015). https://doi.org/10.1007/s10971-014-3477-3
35. X. Xing, L. Du, D. Feng, C. Wang, M. Yao, X. Huang, S. Zhang, D. Yang, J. Mater. Chem. A. **8**, 26004–26012 (2020). https://doi.org/10.1039/d0ta09321a
36. R.L. Palomino-Resendiz, A.M. Bolarín-Miró, F. Pedro-García, F. Sánchez-De Jesús, J.P. Espinós-Manzorro, C.A. Cortés-Escobedo, Ceram. Int. **48**, 14746–14753 (2022). https://doi.org/10.1016/j.ceramint.2022.02.011
37. D. Wang, D. Zhang, Q. Mi, Sens. Actuators, B. **350**, 130830 (2022). https://doi.org/10.1016/j.snb.2021.130830
38. D. Zhang, X. Zong, Z. Wu, Y. Zhang, ACS. Appl. Mater. Interfaces. **10**, 32631–32639 (2018). https://doi.org/10.1021/acsami.8b08493
39. D. Hu, B. Han, R. Han, S. Deng, Y. Wang, Q. Li, Y. Wang, New. J. Chem. **38**, 2443–2450 (2014). https://doi.org/10.1039/c3nj01482g
40. J.K. Srivastava, P. Pandey, V.N. Mishra, R. Dwivedi, J. Nat. Gas Chem. **20**, 179–183 (2011). https://doi.org/10.1016/s1003-9953(10)60168-5
41. H. Zhang, Z. Jin, M.-D. Xu, Y. Zhang, J. Huang, H. Cheng, X.-F. Wang, Z.-L. Zheng, Y. Ding, IEEE. Sens. J. **21**, 13041–13047 (2021). https://doi.org/10.1109/jsen.2021.3054654
42. S.C. Wang, X.H. Wang, G.Q. Qiao, X.Y. Chen, X.Z. Wang, N.N. Wu, J. Tian, H.Z. Cui, Rare Met. **41**, 960–971 (2022). https://doi.org/10.1007/s12598-021-01846-6
43. R. Zhao, Z. Wang, T. Zou, Z. Wang, Y. Yang, X. Xing, Y. Wang, Chem. Lett. **47**, 881–882 (2018). https://doi.org/10.1246/cl.180296
44. C. Zhang, Y.C. Huan, Y. Li, Y.F. Luo, M. Debliquy, J. Adv. Ceram. **11**, 379–391 (2022). https://doi.org/10.1007/s40145-021-0530-x
45. S. Zhang, H.Y. Xiao, S.M. Peng, G.X. Yang, Z.J. Liu, X.T. Zu, S. Li, D.J. Singh, L.W. Martin, L. Qiao, Phys. Rev. Appl. **10**, 044004 (2018). https://doi.org/10.1103/PhysRevApplied.10.044004
46. C. Jin, H. Kim, S. Park, H.W. Kim, S. Lee, C. Lee, Ceram. Int. **38**, 6585–6590 (2012). https://doi.org/10.1016/j.ceramint.2012.05.043
47. H.J. Kim, J.H. Lee, Sens. Actuators, B **192**, 607–627 (2014). https://doi.org/10.1016/j.snb.2013.11.005
48. T. Tong, J. Chen, D. Jin, J. Cheng, Mater. Lett. **197**, 160–162 (2017). https://doi.org/10.1016/j.matlet.2017.03.091
49. G. Dong, H. Fan, H. Tian, J. Fang, Q. Li, Rsc Adv. **5**, 29618–29623 (2015). https://doi.org/10.1039/c5ra01869b

50. H.X. Xu, J.H. Xu, J.L. Wei, Y.M. Zhang, Materials. **13**, 3829 (2020). https://doi.org/10.3390/ma13173829
51. Z. Ling, C. Leach, Sens. Actuators, B. **102**, 102–106 (2004). https://doi.org/10.1016/j.snb.2004.02.017